Synthesis And Investigation Of Some Triple Perovskite Ruthenates

A thesis submitted towards partial fulfilment of
BS-MS Dual Degree Programme

by

Kaustav Dey

under the guidance of

Dr. Sunil Nair

Assistant Professor

Indian Institute of Science Education and Research
Pune

Certificate

This is to certify that this thesis entitled **Synthesis And Investigation Of Some Triple Perovskite Ruthenates** submitted towards the partial fulfillment of the BS-MS dual degree programme at the Indian Institute of Science Education and Research Pune, represents original research carried out by **Kaustav Dey** at **Indian Institute of Science Education and Research Pune**, under the supervision of **Dr.Sunil Nair** during the academic year 2015-2016.

Kaustav

Student
NAME
KAUSTAV DEY

Supervisor
NAME
DR. SUNIL NAIR

1.pdf

Declaration

I hereby declare that the matter embodied in the report entitled **Synthesis And Investigation Of Some Triple Perovskite Ruthenates** are the results of the investigations carried out by me at the Department of Physics, Indian Institute Of Science Education And Research,Pune, under the supervision of Dr.Sunil Nair and the same has not been submitted elsewhere for any other degree.

Kaustav

Student
NAME

KAUSTAV DEY

Supervisor
NAME

Dr. SUNIL NAIR

(1).pdf

Acknowledgements

- I take this opportunity to express my gratitude and sincere thanks to my supervisor, Dr.Sunil Nair for giving me this opportunity to work in his lab. I am grateful for his constant support and inspiring guidance.
- I would also like thank the Director of IISER PUNE, Dr. K. N. Ganesh for his support and all the faculty members of IISER PUNE for their motivation.
- I would like thank Dr.Jitender Thakur(post doc), for his constant support, fruitful discussions and for all the help that he has given me especially with the dielectric measurements.
- I would like to thank my lab members Soumendranath for the discussions, Sarath, Rohit for political and fitness related discussions, Avirup for motivating and helping me throughout the project. Thanks to Charu and Deepak for introducing me to the lab during the start of my project. Thanks to Devika for constant entertainment in the lab.
- I would like to thank Dr. Surjeet Singh and all his lab members Rabindranath Bag, Prachi Telang and Giri for helping me with the heat capacity measurements.
- I would like to thank Dr. A.K. Nigam, for the field dependent heat capacity measurements.
- I would like to thank the technical staff of H cross, Nilesh Dumbare, Prashanth Kale, Anil Shetty and T.S. Yatish for there support.
- I would like to thank all my friends Arjun, Anur, Abhishek, Smita, Phani and all my other batchmates for the all the good times that we have had at IISER.
- I would like to thank Sumit Bhaiya, Rahul Biradar, Aditya Kabra for always being there during the tough times.
- I would like to thank Sanskruti Gaikwad for beign there with me in everything.
- I would like to thank my sister and my brother in law for the weekend fun and for taking my mind away from research at times.

- Finally, I would like to thank my mom and dad for their immense support and IISER for giving me such a platform, motivating me to do research.

Abstract

$Ba_3CoRu_2O_9$ and $Ba_3BiRu_2O_9$ are triple perovskite ruthenates crystallizing in a hexagonal structure. These are among the very few oxides which have ruthenium in unusually high oxidation state of $+5$. Investigations of systems with such high oxidation state of ruthenium has been limited. Magnetic and dielectric investigations have been done on these synthesized polycrystalline samples. We observe possible signature of strong magneto-dielectric coupling with a sharp drop of dielectric susceptibility across the magnetic transition temperature along with relaxor like behavior for $Ba_3BiRu_2O_9$. C_p/T^3 vs T plot shows deviation from the expected Debye behavior, exhibiting qualitative features of a magnetic glass.

Contents

1 Introduction **4**
- 1.1 Ferroelectrics . . . 4
  - 1.1.1 Relaxors . . . 5
- 1.2 Multiferroics . . . 6
  - 1.2.1 Type I Multiferroics . . . 7
  - 1.2.2 Type II Multiferroics . . . 8
- 1.3 Triple Perovskite Ruthenates . . . 11
  - 1.3.1 Multiferroicity in $Ba_3NiNb_2O_9$ . . . 13
  - 1.3.2 Possible charge ordering in $Ba_3NaRu_2O_9$ . . . 13
  - 1.3.3 Orbital ordering in $Ba_3CoRu_2O_9$ . . . 14
  - 1.3.4 Magnetoelastic transition in $Ba_3BiRu_2O_9$ . . . 15
- 1.4 Plan of the thesis . . . 15

2 Methods **18**
- 2.1 Sample Preparation . . . 18
- 2.2 Structural Analysis Using X-Ray Diffraction . . . 19
- 2.3 Magnetic Measurements . . . 20
- 2.4 Dielectric Spectroscopy . . . 21
- 2.5 Scanning Electron Microscopy (SEM) . . . 22
- 2.6 Heat Capacity Measurement . . . 23

3 Magnetic And Electric Properties in $Ba_3CoRu_2O_9$ **26**
- 3.1 X-Ray Powder Diffraction And Rietveld Refinements . . . 26
- 3.2 Magnetic Properties . . . 26
- 3.3 Specific Heat . . . 32
- 3.4 Dielectric Measurements . . . 34

4 Magnetic And Electric Properties in $Ba_3BiRu_2O_9$ **36**
- 4.1 X-Ray Powder Diffraction And Rietveld Refinements . . . 36
- 4.2 Magnetic Measurements . . . 36
- 4.3 Specific Heat Measurements . . . 39

4.4 Dielectric Measurements 40

5 Summary And Future Work **44**
5.1 Summary 44
5.2 Future Plans 45

References **46**

Chapter 1

Introduction

1.1 Ferroelectrics

Ferroelectrics are materials which have a permanent electrical polarization, which could be switched by switching of the direction of the electric field. Analogous to the ordering of magnetic spins in a ferromagnet, ferroelectricity is due to the long range order of electrical dipoles in a material. Usually ferroelectricity is the presence of spontaneous polarization in the material which may be due to geometric reasons as in $BaTiO_3$ [1] or an order-disorder driven as in KH_2PO_4 [2].

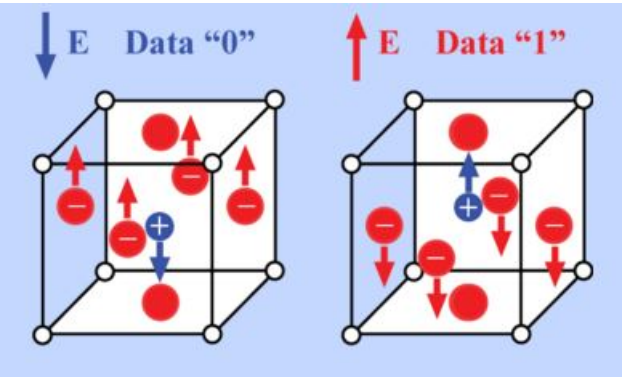

Figure 1.1: Dipoles are ordered in ferroelectrics. The dipoles change the direction upon reversing the direction of electric field(E). Data "0" and Data "1" represents the electric field in the opposite directions. *http* : *//www.devicemodeling.com/research.html*

1.1.1 Relaxors

Relaxors are materials which unlike ferroelectrics, lack long range order. Since the discovery of Relaxor ferroelectrics, it has received special attention due to its unusual dielectric behavior[3]. Typical behavior of the dielectric constant with respect to temperature is as shown in the fig1.2. With the increase in frequency the maximum in the dielectric constant decreases. Frequency dependence of dielectric constant is attributed to the formation of polar nano regions (PNRs) [4]. PNRs are the clusters with individual dipole moment, which are formed in the material below a certain temperature known as the Burn's temperature(T_b) [4]. PNRs are dynamical in nature with thermally fluctuating dipole moment.

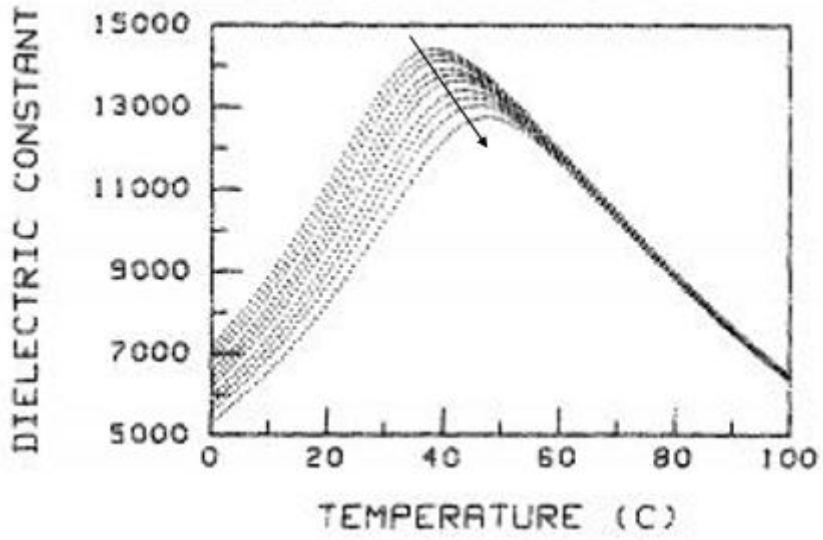

Figure 1.2: Temperature dependence of dielectric constant with respect to temperature at various frequencies. Plot showing typical behavior of relaxor ferroelectrics[3]. With the increase in frequency the maximum in the dielectric constant decreases.

T_b in general is higher than the temperature of maximum real dielectric permittivity(T_m)[5]. On cooling the number of the PNRs increase along with increase in their size [5]. This increase in size of the PNRs is due to increase in correlation between them. The correlations increase up to a temperature known as freezing temperature (T_f) below which PNRs are said to be frozen leading to negligible contribution to dielectric susceptibility [5]. The number of PNRs able to follow the switching in electric field decreases with increase in frequency, hence the maximum in real dielectric susceptibility decreases

with frequency[3], as can be seen in the fig1.2.

Dielectric Relaxation can be modeled by in analogy to the more extensively investigated spin-glass systems[3]. The relaxation in these systems can be described by the Vogel-Fulcher relationship.

$$\omega = f_o exp[-E_a/k(T_{max} - T_f)] \tag{1.1}$$

where T_f is the static freezing temperature,
E_a is the activation energy,
f_o is the Debye frequency,
T_{max} is the temperature of the permittivity maximum.
The Vogel-Fulcher relation is the normal Debye relaxation also known as the single relaxation time model with a temperature dependent ac- activation energy[3].

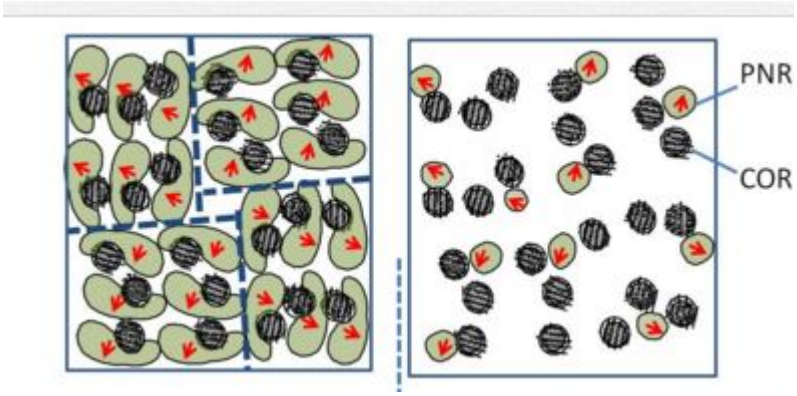

Figure 1.3: Picture on the left shows a ferroelectric forming long range order and domains. On the right we could see the PNRs which lack long range order leading to a relaxor ferroelectric[6].

1.2 Multiferroics

Multiferroics are materials in which magnetism and ferroelectricity coexist at a particular temperature [7]. Magnetism is related to the interactions and ordering of the spins whereas ferroelectricity is due to the ordering of electrical dipoles. Huge interest in multiferroic research is driven by the high technological applicability of these materials. Of particular interest is the cross-coupling between magnetic and electric orders termed as magneto-electric coupling[8]. Coexistence of magnetism and polarization can lead to

the realization of four state-logic in a single material[9]. One of the other applications include magnetically field-tuned capacitors in which frequency dependence of electronic circuits could be tuned with magnetic fields[10].

Multiferroics are rare, because it has been argued that the presence of

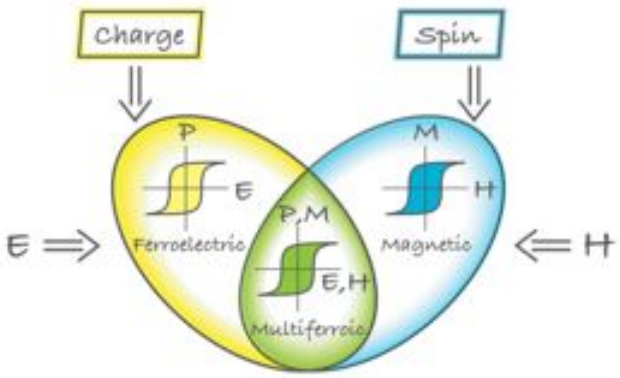

Figure 1.4: Schematic showing that the materials which are ferroelectric and has magnetic order fall under the category of Multiferroics.

unpaired electrons in the d-orbitals of transition metals which is necessary for magnetism inhibits hybridization with the p-orbitals of the surrounding oxygen ions thus inhibiting cation displacement, which is necessary for ferroelectricity[10]. This is commonly known as d^0/d^n mutual exclusivity in a material[11]. Based on the difference in microscopic origin of ferroelectricity, multiferroics are broadly classified into two categories as type-I and type-II.

1.2.1 Type I Multiferroics

Type I multiferroics are those materials in which the sources of ferroelectricity and magnetism are independent of each other with very little coupling in between them. In these materials, ferroelectricity typically takes place above magnetic ordering temperature, and could also be above room temperature. The spontaneous polarization is of the order of $\sim 10-100\mu C/cm^2$[12]. These multiferroics are older and more numerous and a major area of research is to increase the coupling between magnetism and ferroelectricity[12]. Depending on their microscopic mechanisms, type I multiferroics can be classified in the following classes:

- 1.**Ferroelectricity due to lone pairs**
  In $BiFeO_3$, the outer $6s$ electrons do not participate in bonding, form-

ing lone pairs. The ordering of these high polarizibility lone pairs leads to ferroelectricity in $BiFeO_3$[12]. A similar mechanism is responsible for the origin of ferroelectricity in $PbVO_3$.

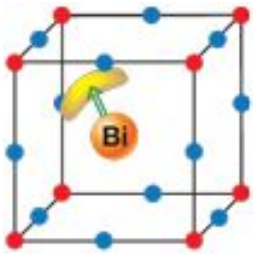

Figure 1.5: In $BiFeO_3$ the ordering of lone pairs contribute to the ferroelectricity[12].

- 2.**Ferroelectricity due to charge ordering**

  The mechanism by which charge ordering may lead to ferroelectricity is shown in the fig1.6. When both bond center(C) and site centered(B) charge ordering takes place in a material (D), then a finite polarization is induced due to the non-centrosymmetry in the material[13].
  This kind of mechanism works in half doped manganates such as $Pr_{.5}Ca_{.5}MnO_3$[12].

- 3.**Geometric Ferroelectricity**

  Ferroelectricity in $YMnO_3$ occurs due to the tilting of of MnO_5 block. This tilting occurs to provide closer packing ,which results in moving of oxygen ions closer to Y, leading to polarization[12].

1.2.2 Type II Multiferroics

The biggest area of interest in multiferroics lies in the the search of type II multiferroics in which ferroelectricity exists in a magnetically ordered state and is caused by only a particular type of magnetism [12]. Due to the coupling of electrical and magnetic orders in a material, type II multiferroics have huge technological applications such as memory devices, magneto-optical devices etc. This coupling (also known as magnetoelectric coupling) studied till date are too small, and the working temperatures are too low for practical applications[14].
Depending on the microscopic mechanism, one can divide type-II multiferroic behavior into two groups:

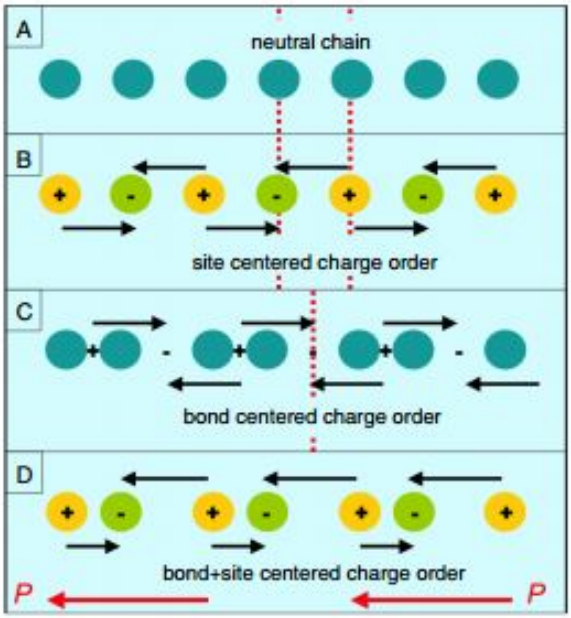

Figure 1.6: Different mechanisms of charge ordering. (A)One dimensional chain, (B)site centered charge ordering, (C)bond-centered charge ordering and (D)a linear combination of these two leads to ferroelectricity.[13].

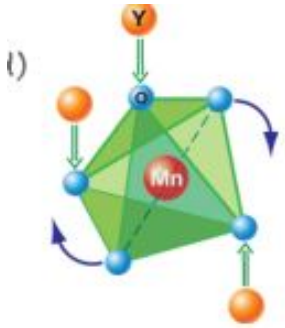

Figure 1.7: The geometric mechanism of generation of polarization in $YMnO_3$[12].

- 1.**Multiferroics with collinear magnetic structure**
  Collinear magnetic moments refers to the alignment of the magnetic moments along an axis. For example in the orthorhombic RMn_2O_5, Mn spins are arranged as $Mn^{+4} - Mn^{+3} - Mn^{+3} - Mn^{+4} - Mn^{+3}$ with anti-ferromagnetic coupling between the nearest neighbor spins. This leads to frustration in the system. Ferroelectricity in these systems is due to exchangestriction. The exchangestriction shifts ions in a way that optimizes spin-exchange energy. In exchangestriction, ions with anti-parallel spins are pulled together whereas ions with parallel spins move away from each other. This leads to non-centrosymmetry in the systems, giving rise to finite polarization[7]. Similar mechanism also takes places in Ca_3CoMnO_6 in which exchangestriction arises from transition metal ions with different valence ($Co^{+2} and Mn^{+4}$)[12].

- 1.**Ferroelectricity in spiral spin structure**
  In a spiral spin structure the spin vectors lie within a plane such that its components along two perpendicular axes on the plane have a periodic variation[14]. The fig1.8 below depicts collinear sinusoidal (a) and various non-collinear spiral magnetic structures. S_i, S_j depicts the spin at neighboring sites i, j and e_{ij} is the unit vector connecting the neighboring sites i and j. Magnetic frustration is the main reason for this kind of magnetic structures[12].

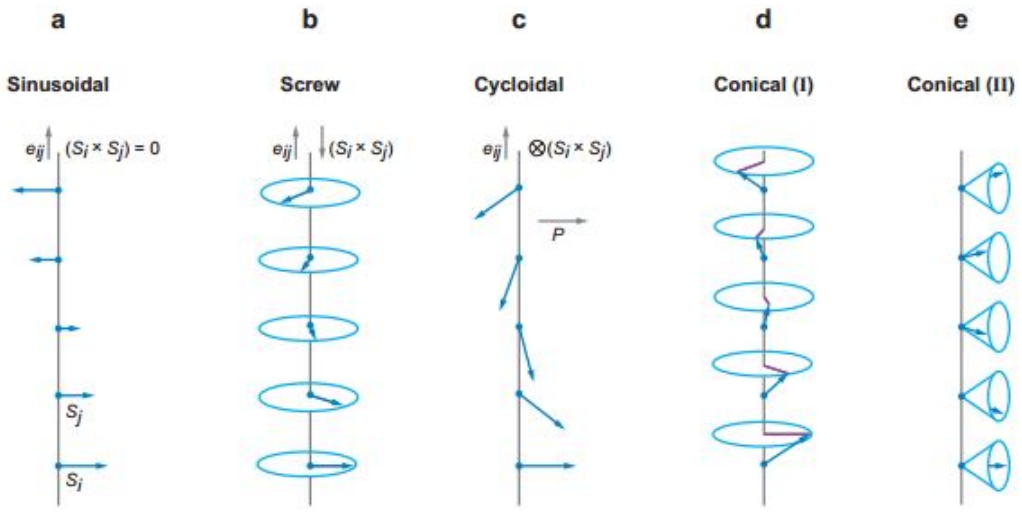

Figure 1.8: Types of magnetic structure.(a)Sinusoidal,(b)Srew, (c)Cycloidal and (d,e)Conical structures[15].

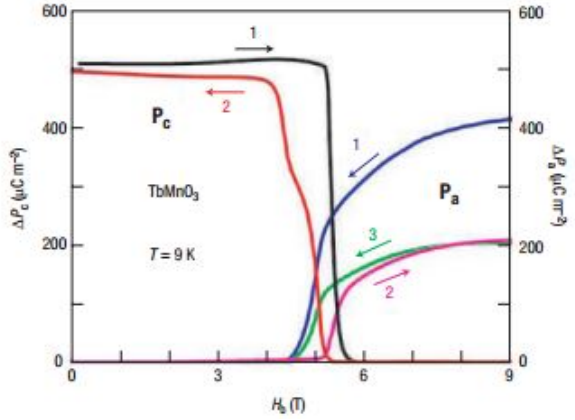

Figure 1.9: Electric polarization in the perovskite $TbMnO_3$ versus magnetic field along b axis. The magnetic field of $\sim 5T$ shifts the direction of polarization from c axis to a axis[7].

Using an phenomenological approach, theoretical studies have shown that electric polarization($\overrightarrow{P}$) and magnetic moments in a system with spiral magnetic structures is described by the equation [16].

$$\overrightarrow{P} = \gamma \overrightarrow{e_{ij}} * [\overrightarrow{S_i} * \overrightarrow{S_j}] \tag{1.2}$$

γ is the constant proportional to spin-orbit coupling and super exchange interactions. The equation 1.2 indicates that finite polarization can appear in non collinear spin structures with spin rotation axis non-parallel to the propagation vector[16]. One of the very famous example of induced ferroelectricity due to spiral magnetic order is $TbMnO_3$[15]. The onset of ferroelectricity in $TbMnO_3$ is due to the appearance of spiral magnetic ordering at $\sim 28K$. In applied magnetic fields, $TbMnO_3$ shows a spin flop transition, at which polarization vector rotates by 90^o[7].

1.3 Triple Perovskite Ruthenates

Given the compositional flexibility, complex magnetic and electrical properties, perovskites are the most studied group of oxides known. The structure of cubic perovskites ABO_3 consists of corner sharing BO_6 octahedra with A cation occupying the 12 fold coordination site.

As shown in the fig1.10, $BaTiO_3$ crystallizes in perovskite structure, in which barium(Ba) occupies the corners, Oxygen(O) occupies the face centers and titanium is in the body center position of the cubic unit cell. 2H-hexagonal variant consists of face sharing octahedra separated by chains of A cations. The structure is similar to the perovskites but the B site is occupied by two different cations, leading to the doubling of the unit cell. For example Sr_2FeMoO_6 as shown in fig1.11 where the B site is occupied by Fe and Mo. Hence these compounds are known as double perovskites. Triple perovskites $A_3BB'_2O_9$ contains corner sharing octahedra interconnected with face sharing bi-octahedra[17]. Triple perovskites generally crystallize in $P6_3/mmc$ space group in hexagonal structure.

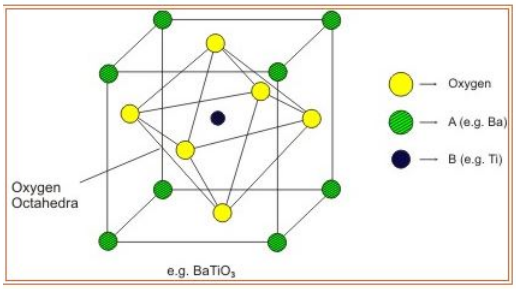

Figure 1.10: Perovskite structure.

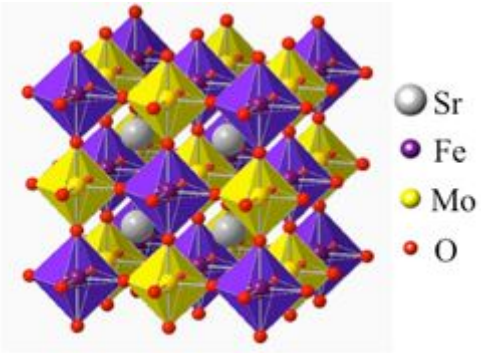

Figure 1.11: Double perovskite lattice.

Ruthenium based oxides have attracted immense attention due to the variety of electronic and magnetic properties. For example superconductivity in Sr_2RuO_4[18] with $T_c = 0.93K$, orbital ordering transition in $La_4Ru_2O_{10}$[19], $CaRuO_3$ showing antiferromagnetic metallic properties[20], spin-gapped haldane phase in $Tl_2Ru_2O_7$[21] and non-Fermi liquid behavior in $La_4Ru_6O_{19}$[22].

The orbital, charge and spin coupling in the ruthenates leads to plethora of properties. So far, the study on ruthenate systems is primarily focused on materials containing Ru^{+4} ions. Studies on ruthenates in high oxidation states such as Ru^{+5} and Ru^{+6} has been limited due to difficulty in their synthesis[23]. Some of the studied Ru^{+5} systems include Li_3RuO_4[24] and $Hg_2Ru_2O_7$, which has a simultaneous magnetic and metal-insulator transition[25]. Some of the interesting properties of

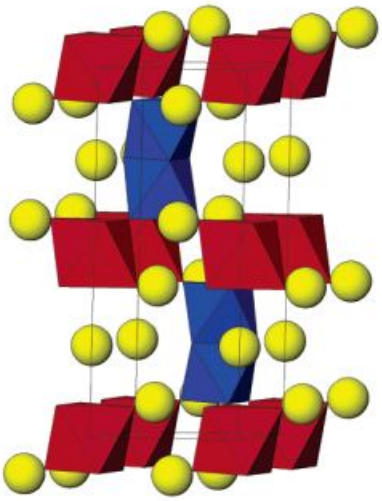

Figure 1.12: Triple perovskite structure with face sharing bi-octahedra (formed by sharing of RuO_6 octahedron) shown in blue, interconnected by corner sharing octahedra (CoO_6) shown in red.[17].

triple perovskites have been reviewed below.

1.3.1 Multiferroicity in $Ba_3NiNb_2O_9$

$Ba_3NiNb_2O_9$ crystallizes in the hexagonal $P-3m1$ structure, and is a quasi-two dimensional spin-one triangular lattice antiferromagnet. At low T, with increase in magnetic field the system evolves from a 120 degree magnetic ordering phase to an up-up-down phase and finally to an oblique phase. The dielectric constant versus temperature plot at various magnetic fields show anomalies (see fig1.13). This is because ferroelectricity switches on each phase boundary with the appearance of spontaneous polarization. One of the possible explanations for the ferroelectric phase in $Ba_3NiNb_2O_9$ at high magnetic fields is the breaking of space inversion symmetry via magnetostriction[26].

1.3.2 Possible charge ordering in $Ba_3NaRu_2O_9$

$Ba_3NaRu_2O_9$ is a mixed-valent triple perovskite which crystallizes in the hexagonal space group $P63/mmc$. In $Ba_3NaRu_2O_9$, ruthenium is present in Ru^{+5} and Ru^{+6} disordered on a crystallographic site.

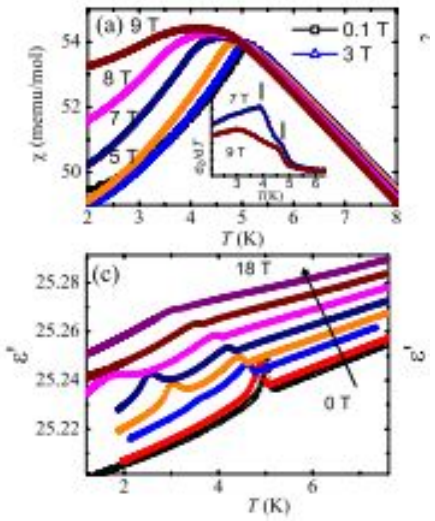

Figure 1.13: (a) Shows the susceptibility dependence versus temperature for $Ba_3NiNb_2O_9$ at various fields. The inset shows $d\chi/dT$ at 7T and 9T. (c) Temperature dependence of real dielectric constant versus temperature at 0, 4, 8, 10, 12, 16, 18 T[26].

The plot 3.1 shows the magnetic susceptibility dependence on temperature. $Ba_3NaRu_2O_9$ undergoes a structural transition to orthorhombic $Cmcm$ space group at 225K. There is an abrupt decrease in susceptibility at 210K followed by a steady decrease in susceptibility with decreasing temperature. On the basis of analysis of Ru-Ru bond distance it has been commented that structural transition involves charge ordering of Ru^{+5} and Ru^{+6}[17].

1.3.3 Orbital ordering in $Ba_3CoRu_2O_9$

$Ba_3CoRu_2O_9$ is a triple perovskite which crystallizes in the hexagonal space group $P63/mmc$. Structure consists of face sharing RuO_6 octahedra forming $Ru_2^{+5}O_9$ dimers interconnected by CoO_6 octahedra. $Ba_3CoRu_2O_9$ undergoes a structural transition from hexagonal to orthorhombic along with a change in magnetic moment corresponding to S=3/2 to S=1/2. This is due to the formation of singlet state in one of the orbitals, resulting in lifting of orbital degeneracy[23]. Due to the structural transition, the Ru-O bond lengths change due to the repulsion between Ru d and O p orbitals[23] (see fig1.15). This is because orbitals arrange in a certain fashion to reduce repulsion along a axis.

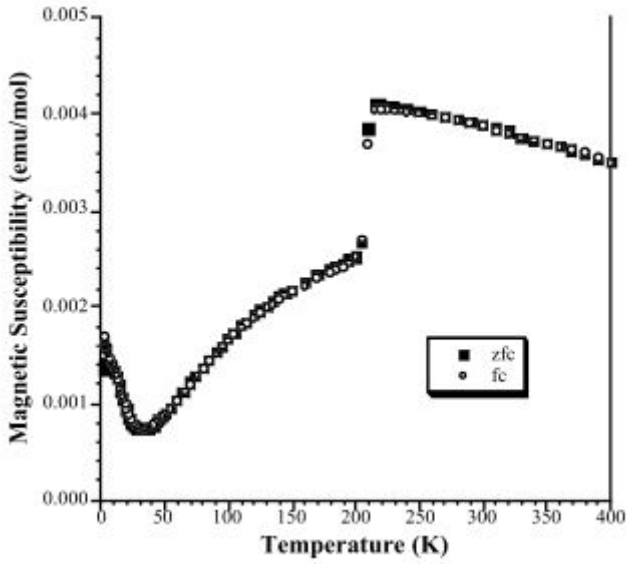

Figure 1.14: Plot of susceptibility versus temperature for $Ba_3NaRu_2O_9$[17].

Hence their is an orbital ordering transition in the $Ru_2^{+5}O_9$ dimers[23].

1.3.4 Magnetoelastic transition in $Ba_3BiRu_2O_9$

$Ba_3BiRu_2O_9$ has a monoclinic distortion, hence crystallizes in the space group $C2/c$. It contains BiO_6 octahedra sharing vertices with Ru_2O_9 dimers. Measurements on $Ba_3BiRu_2O_9$ reveal a simultaneous magnetic and magnetoelastic transition at 176K[27]. This magnetoelastic transition could be tuned by application of external pressure. Application of pressure of about 600 Mpa reduces the transition temperature to 157K[28] (see fig1.16).

1.4 Plan of the thesis

Due to complex interplay of orbital,charge and spin degrees of freedom there is plethora of interesting properties in these triple perovskite ruthenates. The aim of this thesis is to synthesis the compounds $Ba_3CoRu_2O_9$ and $Ba_3BiRu_2O_9$ in polycrystalline form, by the standard solid state methods. These compounds comprise of ruthenium in

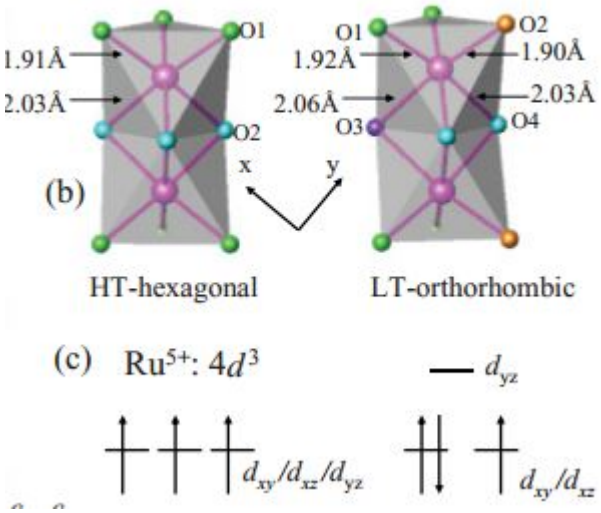

Figure 1.15: (b) Shows the Ru-O bond distance in a $Ru_2^{+5}O_9$ dimer, above (Hexagonal phase) and below(orthorhombic phase) the transition. (c) Shows the corresponding change in the magnetic moment in a t_{2g} orbital of Ru^{+5}[23].

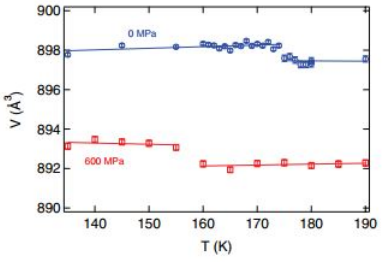

Figure 1.16: Unit cell volume of $Ba_3BiRu_2O_9$ versus temperature at 0 Mpa and 600 Mpa. . The transition shifts to a lower temperature on application pf pressure[28].

unusually high oxidation state. Studies of ruthenates in such high oxidation state has been limited. After synthesis, the aim is to do the complete structural analysis of these compounds along with investigation of magnetic and dielectric properties. To investigate if the dielectric properties are coupled to that of the magnetic properties, if their is a possible magneto-dielectric coupling or if it is a potential multiferroics. We expect to see such a coupling due to the coincidental structural and magnetic transition in both $Ba_3CoRu_2O_9$ and $Ba_3BiRu_2O_9$. To compare how the substitution of magnetic cobalt(Co) atom with non-magnetic bismuth(Bi) affect structural, magnetic and dielectric properties of these systems.

Chapter 2

Methods

2.1 Sample Preparation

The polycrystalline samples were synthesized using the standard solid state route. In this method stoichiometric amount of high purity (almost 99.99% pure) oxides and carbonates of respective elements are thoroughly mixed to form homogeneous mixture by grinding in a mortar and pestle. The homogeneous mixture of about few grams ($\sim 1-4gm$) are kept in the furnace and sintered at temperatures reaching up to 1200°C. Each heat treatment has an average time of $24-48$hours. The samples are further palletized using $13mm$ dye in KBr press(model M-15) before the final treatment.

Table 2.1: The treatment temperatures and time for the synthesized samples of $Ba_3CoRu_2O_9$ and $Ba_3BiRu_2O_9$.

Compound	**Treatment 1/Time**	**Treatment 2/Time**	**Treatment 3/Time**
$Ba_3CoRu_2O_9$	900^oC/24Hrs	1000^oC/24Hrs	1100^oC/24Hrs
$Ba_3BiRu_2O_9$	800^oC/24Hrs	1000^oC/48Hrs	1100^oC/24Hrs

2.2 Structural Analysis Using X-Ray Diffraction

The structural characterization was carried out by performing X-Ray diffraction (XRD) using Bruker D-8 advance with Copper Kα radiation ($\lambda = 1.54\mathring{A}$). The intensity versus 2θ plot of X-Ray diffraction was obtained in the range $10^\circ - 90^\circ$ with a step size of $.01^\circ$. The obtained pattern was analyzed using Rietveld method in FullProf 2000 software. The Rietveld method was first introduced in the year 1967[29]. Since its incorporation it has been widely used technique to analyze the powder XRD data. In the Rietveld method, linear least squares is performed until the best fit is obtained between the experimentally obtained powder diffraction data and the calculated one.
The quantity S_y is minimized in the least squares procedure which is defined as

$$S_y = \Sigma W_i (y_i - y_{ci})^2 \tag{2.1}$$

where $W_i = 1/y_i$
y_i=measured intensity at the i^{th} step
y_{ci}= calculated intensity at the i^{th} step.
The calculated intensity (y_{ci}) is calculated from the given structural model owing to contributions from Bragg reflections along with the background, is given by the equation

$$y_{ci} = s\Sigma_K L_K \left|F_K\right|^2 \phi(2\theta_i - 2\theta_K) P_K A + y_{bi} \tag{2.2}$$

where s is the scale factor,
K indicates the Miller indices (h,k,l) for a Bragg reflection,
L_K represents the Lorentz, Polarization and Multiplicity factors,
ϕ is the profile function,
P_K is the preferred orientation function,
A is an absorption factor,
F_K is the structure factor for the K th Bragg reflection and
y_{bi} is the background intensity at the ith step.
There are several mathematical criteria to judge whether a fit pertaining to global minimum is reached, and not in one of the false minimum. These are given by R-values. The criterion used are

R-weighted pattern

$$R_{wp} = \{\Sigma w_i(y_i(obs) - y_i(calc))^2 / \Sigma w_i(y_i(obs))^2\}^{1/2} \tag{2.3}$$

R-expected

$$R_E = [(N - P)/\Sigma w_i y_{oi}]^{1/2} \tag{2.4}$$

The goodness of Fit indicator (S) is

$$S = [S_y/(N - P)]^{1/2} \tag{2.5}$$

An S value of about 1.3 is considered to be a good fit[30]. A pseudo-Voigt profile function has been used to fit the obtained XRD pattern.

2.3 Magnetic Measurements

The magnetic measurements were done in the Quantum Design Magnetic Property Measurement System (MPMS) magnetometer. A small amount of the sample($\sim 25 - 50mg$) is taken in a capsule which is non-magnetic and is placed at the center of a non-magnetic straw. The straw attached to the holder is inserted into the sample chamber containing superconducting pick up coils. MPMS is a highly sensitive instrument which can detect magnetic moments of about 10^{-8} emu and can go upto 7 Tesla magnetic field.

For the measurements, the sample is positioned in between the superconducting pick up coils, which is situated at the center of superconducting magnet. Any change in magnetic flux in the coil produces current in the loop. The detection coils are connected to the input coil of the superconducting quantum interference device (SQUID). SQUID is extremely sensitive to magnetic field and is based on superconducting loops forming Josephson Junctions. SQUID converts current input into voltage output. So any current in the loop which is generated due to a changing magnetic moment in the sample is proportional to the SQUID voltage output. The voltage output is further converted by a calibrated system, directly into magnetic moment.
In this project DC magnetic measurements were done in the temperature range $2 - 300K$. The measurements are done in Zero-Field Cool

(ZFC) and Field Cooled (FC) mode. In ZFC and FC mode, the temperature of the sample is lowered to 2K with and without a field respectively. The measurements are done by warming the sample from $2K - 300K$.

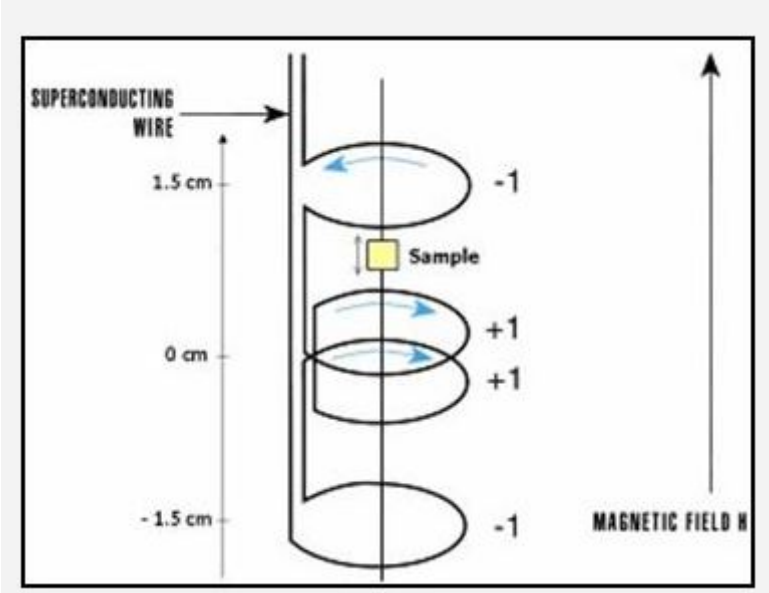

Figure 2.1: Figure showing the sample in the middle of pick up coils. *http* : *//squid.iitd.ernet.in/Basic*$_L$*iterature.htm*

2.4 Dielectric Spectroscopy

The dielectric spectroscopy is a very useful technique in analyzing dynamic response of a material to an applied Electric Field. This technique in principle gives the response of electrical dipoles formed in the material with respect to electric field. It is used to probe various phenomenon like ferroelectricity, dipolar ordering, dipolar relaxation etc. It is used to determine electrical permittivity of the system,ϵ^*.

$$\epsilon^* = \epsilon^{'} - i\epsilon^{"} \tag{2.6}$$

Here $\epsilon^{'}(\epsilon^{"})$ is the real(imaginary) permittivity of the material.
A specimen in the form of a pellet is used for the measurement. Silver paste is applied on both the flat surfaces of the pellet and it is placed

in between two metal electrodes, forming a parallel plate type configuration. A sinusoidal voltage V_s is passed through the sample with the help of a voltage generator, and the current I_s and the phase shift are measured across the sample. The impedance Z^* is calculated using Ohm's law;

$$Z^* = V_s/I_s \tag{2.7}$$

From the impedance we can calculate the sample capacitance, and from the sample capacitance dielectric permittivity is determined by the following equations;

$$C^* = -i/2\pi f Z^* \tag{2.8}$$

$$\epsilon^* = \epsilon^{'} - i\epsilon^{"} = C^* d/\epsilon_0 A \tag{2.9}$$

Measurements are done in 1V excitation. In this project, all the Dielectric measurements are performed in the temperature range of $15K - 300K$. The capacitance of the sample is measured using the Novacontrol Alpha A frequency analyzer operating in the range $3\mu Hz$ to $20Mhz$. The dependence of $\epsilon^{'}(\epsilon^{"})$ with respect to temperature at various frequencies is measured.

2.5 Scanning Electron Microscopy (SEM)

Scanning electron microscope(SEM) is an important tool to obtain information about the surface morphology and composition of the material by scanning through high-energy electrons. As the electron beam hits the specimen, various signals come out as shown in the fig2.2. The SEM utilizes these signals to observe and analyze the specimen surface.

SEM contains an electron optical probe to produce an electron beam, a specimen stage, a secondary electron detector, an image display unit and an operation system to perform various operations. The basic construction of a SEM is shown in the fig2.3. The electron optical probe consists of an electron gun, a condenser lens to adjust the diameter of electron beam and objective lens to focus the beam[31]. The specimen

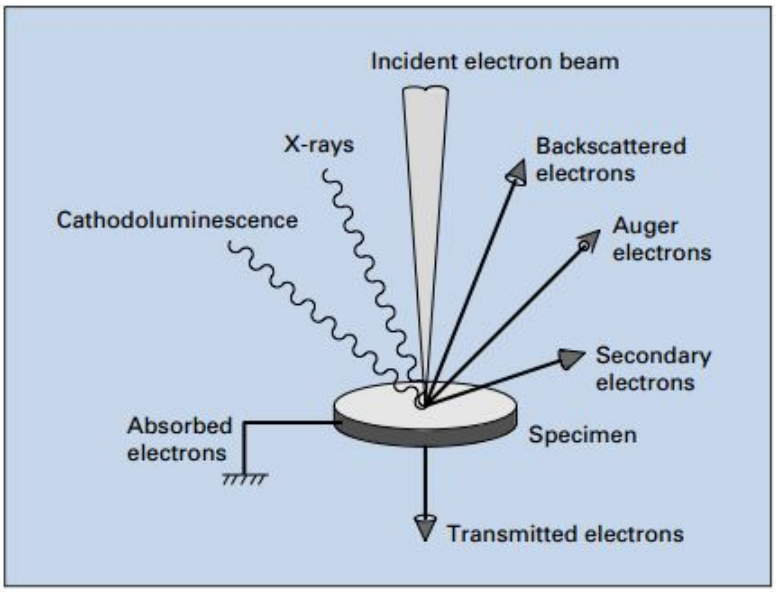

Figure 2.2: Picture showing the emission of various signals from the specimen[31].

stage stably supports the specimen and can make smooth movements in horizontal(X,Y) direction, vertical(Z) direction, tilting(T) and rotation(R). The electron optical pump and the specimen chamber are kept in a vacuum of $\sim 10^{-3} - 10^{-4} Pa$, by the use of a diffusion pump.

When the electron beam enters the specimen, the secondary electrons are produced from the emission of valence electrons of the constituent atoms of the specimen. Secondary electrons are sensitive to the surface. As the energy of the secondary electrons is low, those emitted from within the sample are absorbed. Backscattered electrons also known as reflected electrons, are the electrons that are scattered backwards and emitted out of the sample. Information pertaining to relatively deeper regions is contained in the backscattered electrons, as these are higher in energy than the secondary electrons. Backscattered electrons are sensitive to the composition of the sample. For example the area having an heavier atom appears brighter in a back-scattered image[31].

2.6 Heat Capacity Measurement

Heat capacity measurements provide considerable information about the electronic, lattice and magnetic properties of the materials. Mea-

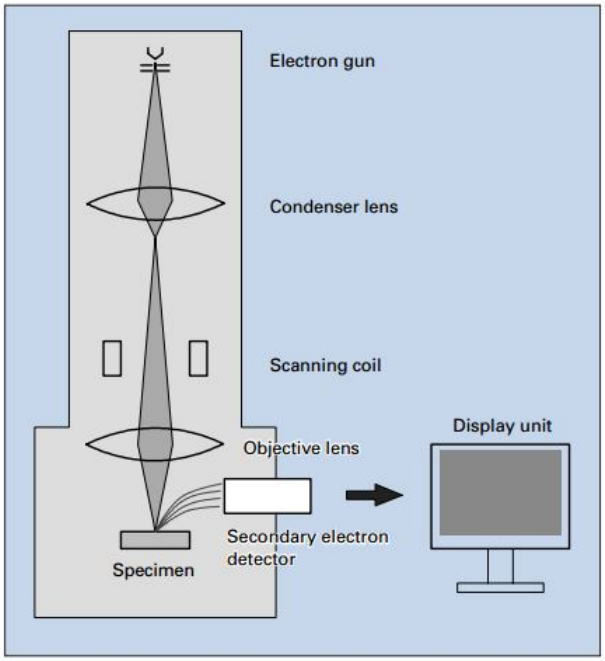

Figure 2.3: Picture showing basic components of a SEM[31].

surements below the Debye temperature allows to directly probe the magnetic and electronic energy levels of the materials[32]. In this project, heat capacity measurements are done in the quantum design physical property measurement system (PPMS), which measures the heat capacity at constant pressure(C_p).

$$C_p = (dQ/dT)_p \tag{2.10}$$

In a particular measurement, a known amount of heat at constant power is supplied for a fixed time, then followed by cooling period for the same time. This method of measurement is known as relaxation method. The sample holder is a platform with an attached heater and thermometer to its bottom (see fig2.4). The sample is mounted on the platform with Apiezon grease, which provides the required thermal contact. The wires connecting platform to the puck frame provide thermal links to the thermal bath. The PPMS turbo pump provides sufficient vacuum($\sim 1mTorr$) so that thermal conductance is dominated by the conducting wires[32].

The measurement is done on the samples weighing approximately 1 to 200 mg, in the temperature range 2K-400K. Assuming a good thermal

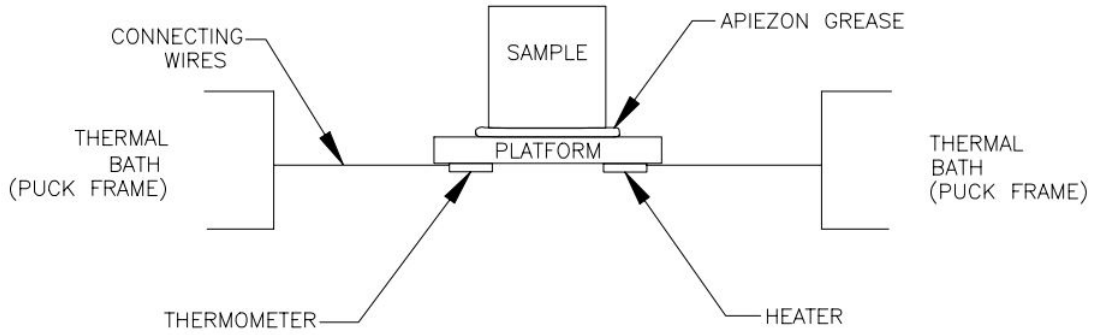

Figure 2.4: Sample holder with the sample in the PPMS heat capacity measurement[32].

contact between the sample and the platform, the temperature T of the platform varies with time t according to the simple model[32]:

$$C_{total}dT/dt = -K_w(T - T_b) + P(t) \tag{2.11}$$

where C_{total} is the total heat capacity of the sample and the sample platform, K_w is the thermal conductance of the supporting wires, T_b is the temperature of the thermal bath, $P(t)$ is the power applied by the heater. The heat capacity of the sample is obtained by subtracting the heat capacity from C_{total} of the sample platform which could be obtained from an addenda measurement.

Chapter 3

Magnetic And Electric Properties in $Ba_3CoRu_2O_9$

3.1 X-Ray Powder Diffraction And Rietveld Refinements

Powder XRD data for $Ba_3CoRu_2O_9$ shows single phase without any impurity peaks and refinement was done using Full Prof software. The fig 3.1 shows the Rietveld refinement of $Ba_3CoRu_2O_9$. From the refinement it is conformed that $Ba_3CoRu_2O_9$ crystallizes in the hexagonal space group $P63/mmc$. The lattice and fitting parameters are shown in the table3.1. The results are in good agreement with the reported data[23]. There are two crystallographic positions of oxygen in Ru_2O_9 dimers. The corresponding bond lengths are $Ru - O1 = 2.032\mathring{A}$, $Ru - O2 = 1.912\mathring{A}$.

The SEM image of $Ba_3CoRu_2O_9$ is shown in the fig3.2. Hexagonal grains are clearly visible in the image. This is due to the internal hexagonal symmetry in the crystal.

3.2 Magnetic Properties

The magnetic properties was measured using the MPMS squid magnetometer. The ZFC-FC measurements was done with respect to temperature at 1000 Oe. The fig 3.3 shows the ZFC plot of $Ba_3CoRu_2O_9$.

Table 3.1: Lattice and fitting parameters from the refinement of $Ba_3CoRu_2O_9$.

Lattice parameters	
a	$5.754\mathring{A}$
b	$5.754\mathring{A}$
c	$14.130\mathring{A}$
$\alpha = \beta$	90^o
γ	120^o

Fitting Parameters	
U	0.061
V	-0.0354
W	0.0164
R_{wp}	4.94
R_p	2.91
Goodness of fit, S	1.69

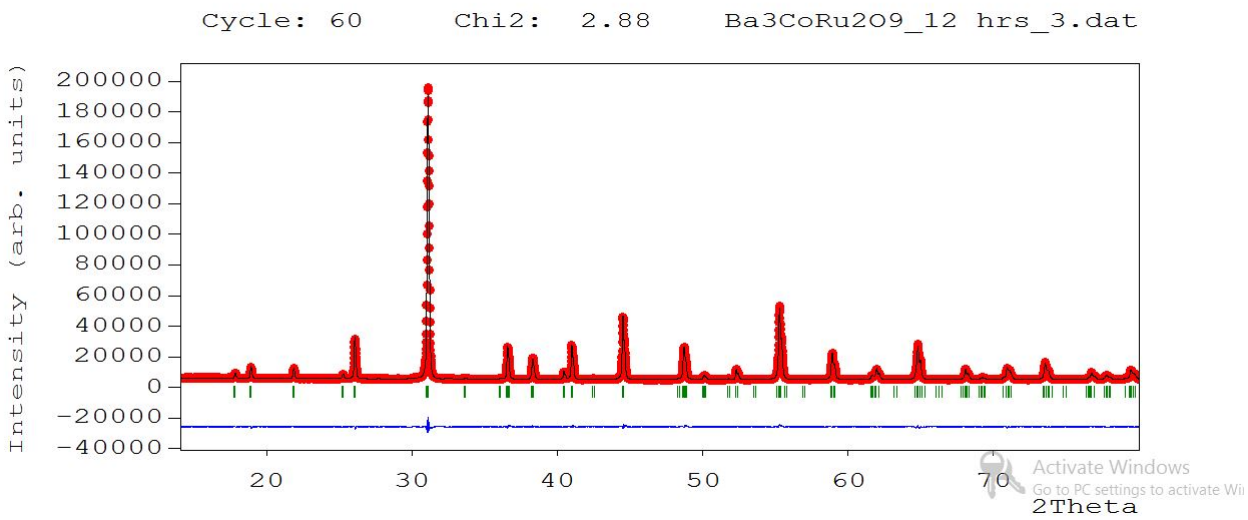

Figure 3.1: Rietveld analysis of XRD pattern of $Ba_3CoRu_2O_9$. Red represents the observed pattern and black represents the calculated pattern. Blue represents the difference between the calculated and experimental.

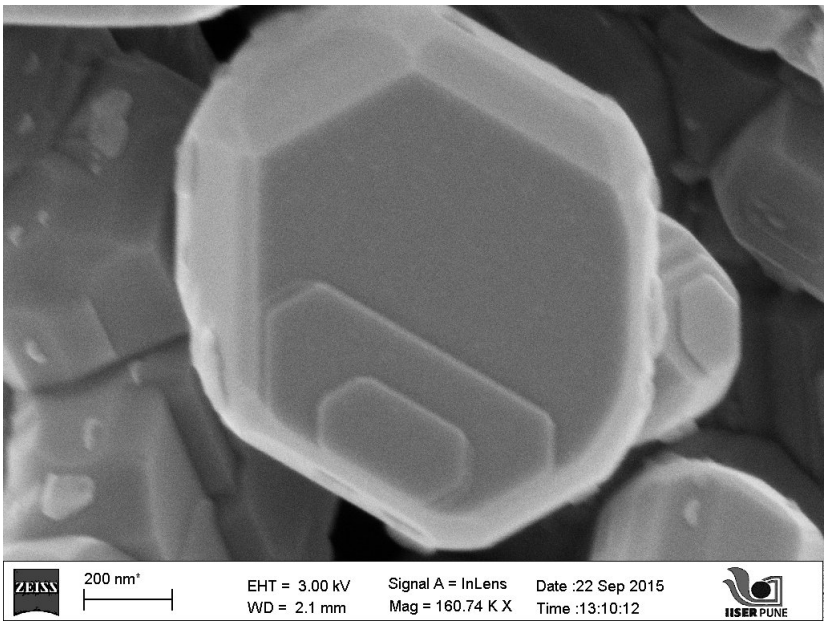

Figure 3.2: SEM image of $Ba_3CoRu_2O_9$. The image shows a hexagonal shaped grain.

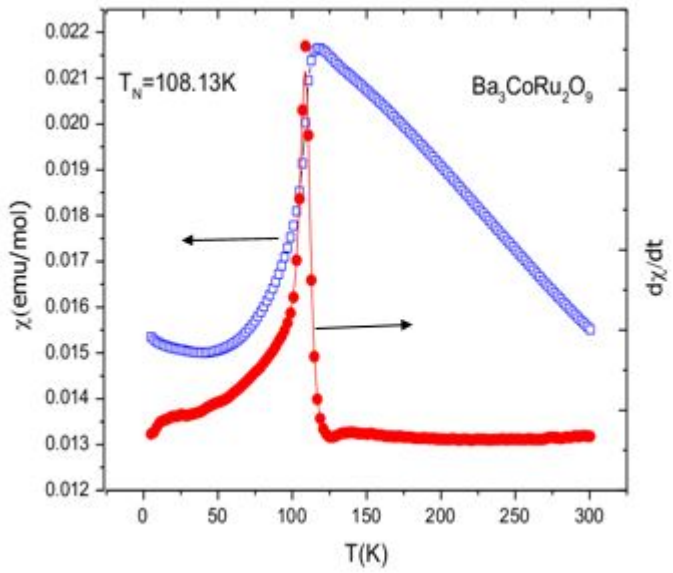

Figure 3.3: ZFC plot of $Ba_3CoRu_2O_9$ versus temperature(in blue). The derivative of susceptibility versus temperature(in red). Transition is at 108.13K

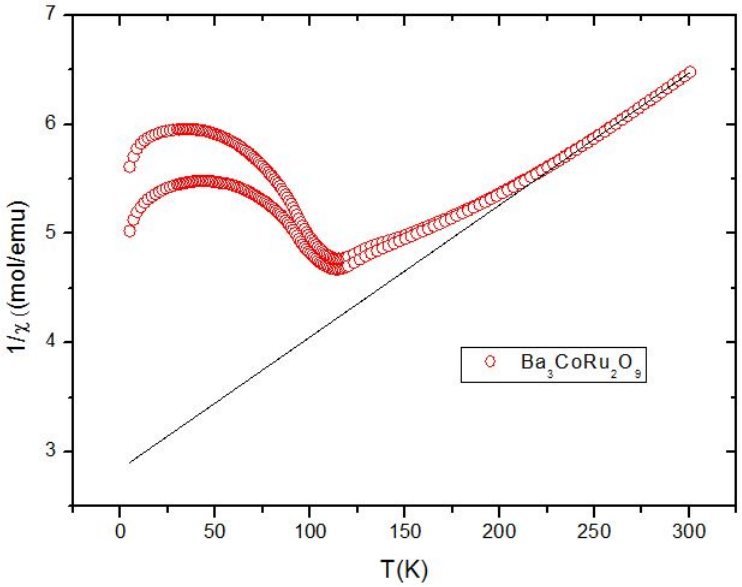

Figure 3.4: Inverse susceptibility versus temperature plot for $Ba_3CoRu_2O_9$. The black line shows the Curie-Weiss (CW) fit. We can see that there is deviation from cw behavior below 225K.

From the fig3.3 we could clearly see that the transition is around 108K. To detect the transition accurately, the derivative of the susceptibility is plotted with respect to the temperature. This is in accordance with the reported data[23]. The transition takes place due to the structural transition from high temperature hexagonal to low temperature orthorhombic structure. The inverse susceptibility dependence on temperature is plotted in the fig3.4. The straight line is the Curie-Weiss(CW) fit in the high temperature. There is a clear deviation from the CW behavior up to 265K. This deviation from the CW behavior is due to the fact that the short range antiferromagnetic correlations still exist above the transition temperature. From the Curie-Weiss fit in the temperature range 265K - 300K, we obtain Neel temperature $T_N = -235K$ and the Curie constant, $C = 82.6$. The calculated effective magnetic moment from the Curie constant is $\mu_{eff} = 2.34\mu_B$.
Neutron diffraction was done in the cold neutron powder diffractometer DMC at the Paul Scherrer Institute(PSI), Switzerland. The measurement was done at $2.45\mathring{A}$ in the temperature range 1.5K to 300K. The Rietveld refinement have been done in the temperature range 175K-300K. On plotting the normalized intensities at various temperature for the (1

0 1) peak, it is observed that there is an additional peak which develops at lower temperature from 175K (see fig3.5), which is higher than the actual magnetic transition(around 108K). This additional peak is likely magnetic in nature. However the Rietveld refinements have to be done below 175K to know the actual magnetic structure. It has to be done by addition of magnetic phase which is unknown. The main transition of para to AFM still exists at 108K. There are extra peaks shown by black arrows in the diffractogram taken at 1.5K which is below ordering temperature(see fig3.6). When there is an anti-ferromagnetic ordering, then the magnetic unit cell at least doubles than that of the crystal unit cell. Hence these leads to extra peaks below the ordering temperature. Refinement was done using the tripled pseudo-Voigt as the peak function. Various instrumental parameters used in the fitting for room temperature neutron data are tabulated in the table 3.2. Refinements below the transition temperature is under progress.

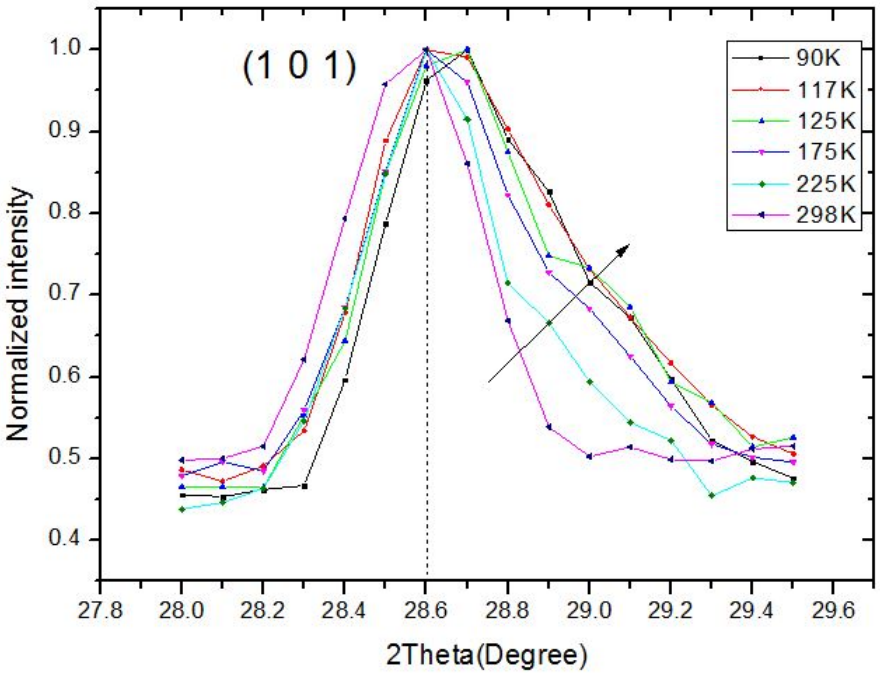

Figure 3.5: Plot showing the normalized intensity versus 2Theta, from the neutron data taken at various temperatures. The arrow points towards the extra peak (magnetic in nature) that develops as the temperature is lowered from 298K, down to 90K.

Table 3.2: Instrumental, Lattice and Fitting parameters obtained from the Reitveld refinement of the room temperature neutron data for $Ba_3CoRu_2O_9$.

Peak Shape	**Tripled pseudo-Voigt**
Instrumental Parameters	
Shape 1	0
X	.2849
Y	.3657
shp1	.00587
C_{thm}	0
Wdt	3
Lattice Parameters	
a	$5.750\mathring{A}$
b	$5.750\mathring{A}$
c	$14.117\mathring{A}$
$\alpha = \beta$	90^o
γ	120^o
Fitting Parameters	
U	1.09
V	-0.5381
W	0.169
R_{wp}	5.75
R_{exp}	2.74
Goodness Of fit, S	1.98

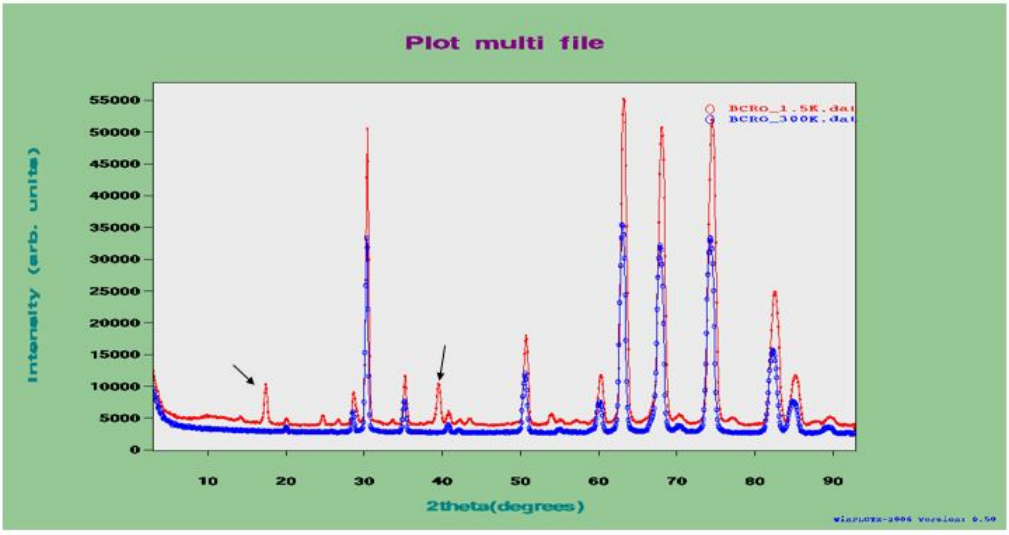

Figure 3.6: The Neutron diffraction patterns at 1.5K and 300K. The black arrow shows the extra peaks appearing at 1.5K, which is below the transition temperature, indicating that these are magnetic peaks.

3.3 Specific Heat

The specific heat dependence on temperature for $Ba_3CoRu_2O_9$ was measured using the PPMS. The dependence is shown in the fig3.7.

There is an anomaly at temperature similar to the magnetic transition temperature. This anomaly is corresponding to the reported[23] transition from high temperature hexagonal to low temperature orthorhombic structure.

Fig 3.7 shows the C_p/T^3 dependence on temperature for $Ba_3CoRu_2O_9$. There is a peak which is visible at around 22K. C_p/T^3 rises below 10K, which is typically non-Debye behavior. According to Debye behavior the specific heat varies as T^3 at low temperatures. This is a characteristic signature of glassy behavior as seen in the half-doped manganites[33]. Although the glassy behavior in the half-doped manganite $Pr_{.5}Ca_{.5}MnO_3$ is due to the destabilized charge ordered state[33], the reason for such a behavior in $Ba_3CoRu_2O_9$ is still unknown.

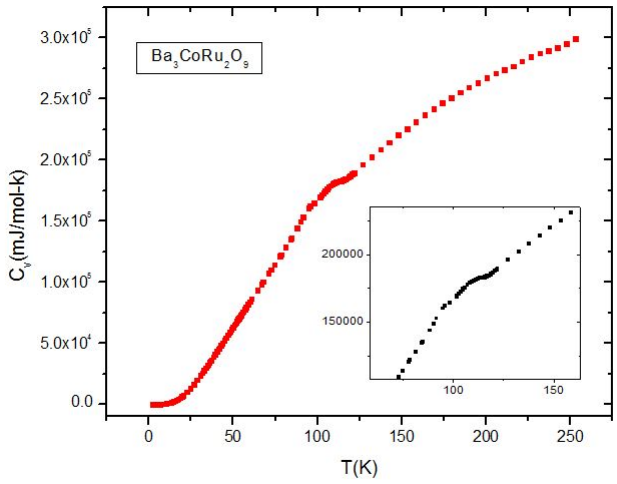

Figure 3.7: Specific Heat versus temperature plot for $Ba_3CoRu_2O_9$.

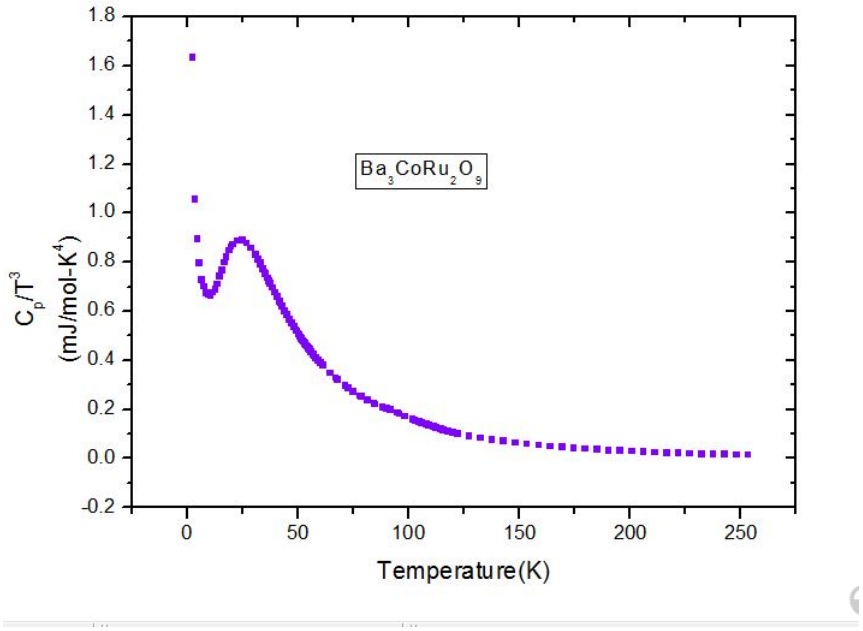

Figure 3.8: C_p/T^3 versus T plot for $Ba_3CoRu_2O_9$.

3.4 Dielectric Measurements

The fig3.9 shows the real part of dielectric constant dependence on temperature at different frequencies for $Ba_3CoRu_2O_9$. The dielectric con-

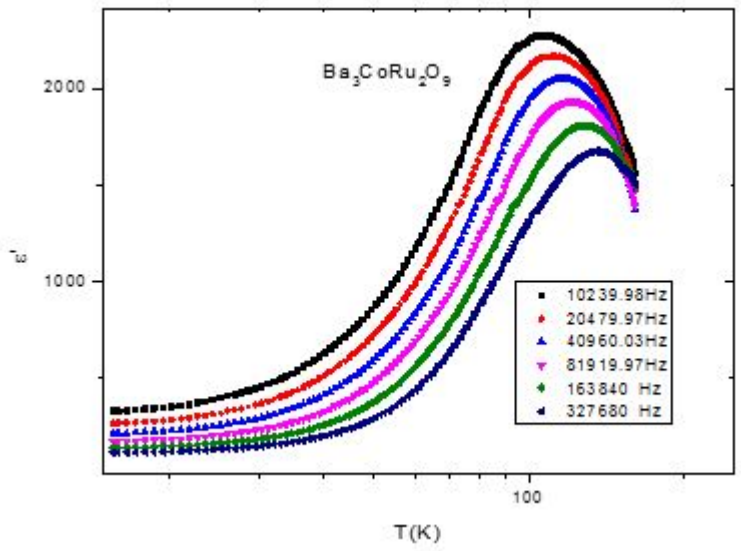

Figure 3.9: Real Dielectric constant versus temperature plot (log scale) for $Ba_3CoRu_2O_9$.

stant decreases rapidly below the transition temperature. This decrease could be due to the change in magnetic structure (paramagnetic to anti-ferromagnetic) leading to the decrease in dielectric constant of the sample. This is also known as magneto dielectric coupling. Although this observation has to be confirmed by doing magneto-dielectric measurements. A typical magneto-dielectric measurement is done by measuring dielectric constant in the presence of magnetic field. We could also see certain frequency dependence above the transition temperature. This kind of frequency dependence arises either due to Relaxor behavior or certain disorder in the system. We tried to do the Vogel-Fulcher fit(VF), which is the frequency dependence on temperature maximum(T_m) from the dielectric spectrum as discussed earlier. All conventional Relaxors follow VF relation. The fit clearly suggested that $Ba_3CoRu_2O_9$ is not a Relaxor ferroelectric. This is also supported by our observation that there is no feature in ϵ'' in this temperature region. The frequency dependence may arise due to some disorder state above the transition temperature or due to existing magnetic correla-

tions above the actual transition temperature. Although this assertion has to be investigated further by refining the neutron diffraction data. In the higher temperatures, above 160K the measured dielectric constant is negative. This is because the sample becomes conducting in this region and a mis-balance in the measuring bridge gives rise to spurious values. Hence the graph has been truncated above this region.

Chapter 4

Magnetic And Electric Properties in $Ba_3BiRu_2O_9$

4.1 X-Ray Powder Diffraction And Rietveld Refinements

Room temperature powder XRD data for $Ba_3BiRu_2O_9$ shows single phase. The Rietveld refinement fit shows that the compound crystallizes in monoclinically distorted space group $C2/c$. The refinement was done using pseudo-Voigt as the peak function. Lattice and various fit parameters are tabulated in the table 4.1. The results are in good agreement with the reported data [27].

The SEM image is shown in the fig4.2. The main difference between the crystal structures of $Ba_3CoRu_2O_9$ and $Ba_3BiRu_2O_9$ is that $Ba_3BiRu_2O_9$ is distorted with the angle beta=91.02.

4.2 Magnetic Measurements

Susceptibility dependence on temperature at $5000Oe$ for $Ba_3BiRu_2O_9$ is shown in the fig.4.3. There is a drastic drop in the susceptibility below $T^* = 176K$. This drastic drop in susceptibility is ascribed to an opening of a gap in the spin excitation spectrum between non-magnetic singlet state and excited triplet spin configurations. It is due to the coincidental structural and magnetic dimerization[27]. Above the transition temperature the susceptibility is seen to increase. This increase is

Table 4.1: Lattice and fitting parameters from the Rietveld fit of $Ba_3BiRu_2O_9$.

Lattice parameters	
a	5.939$\mathring{A}$
b	10.276$\mathring{A}$
c	14.733$\mathring{A}$
α	90^o
β	91.02^o
γ	120^o
Fitting Parameters	
U	0.213
V	-0.284
W	0.170
R_{wp}	18.9
R_p	31.8
R_{exp}	13.68
Goodness of fit, S	1.38

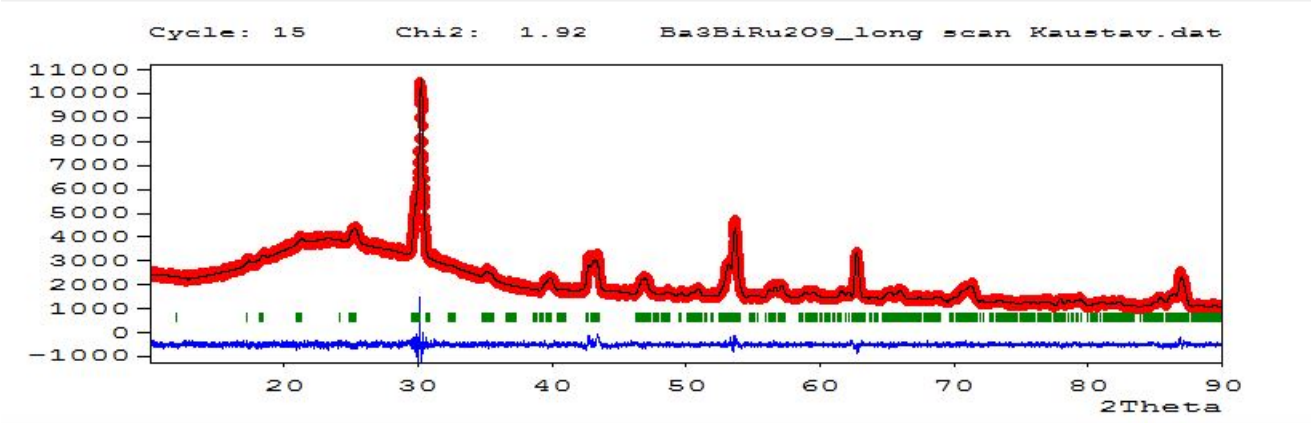

Figure 4.1: Rietveld analysisof XRD pattern of $Ba_3BiRu_2O_9$. Red represents the observed pattern and black represents the calculated pattern. Blue represents the difference between the calculated and experimental.

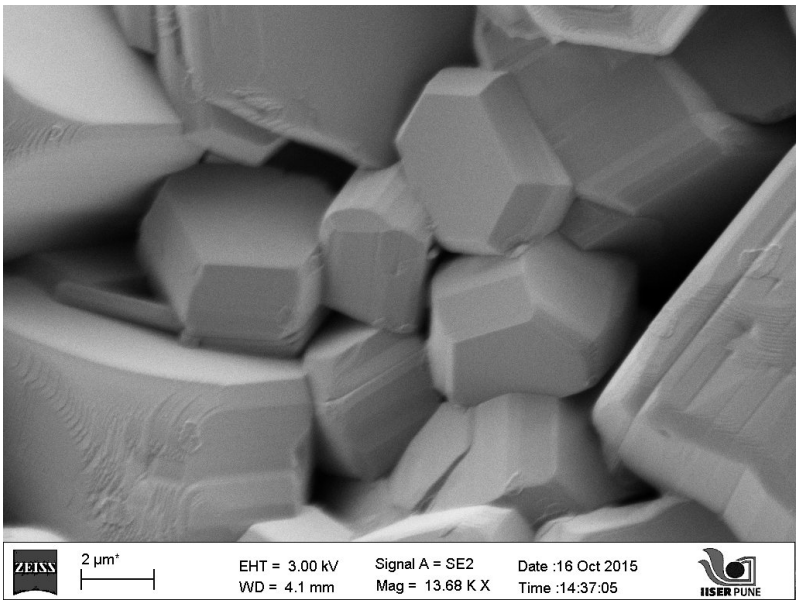

Figure 4.2: SEM image of $Ba_3BiRu_2O_9$. The image showing hexagonal shaped crystals.

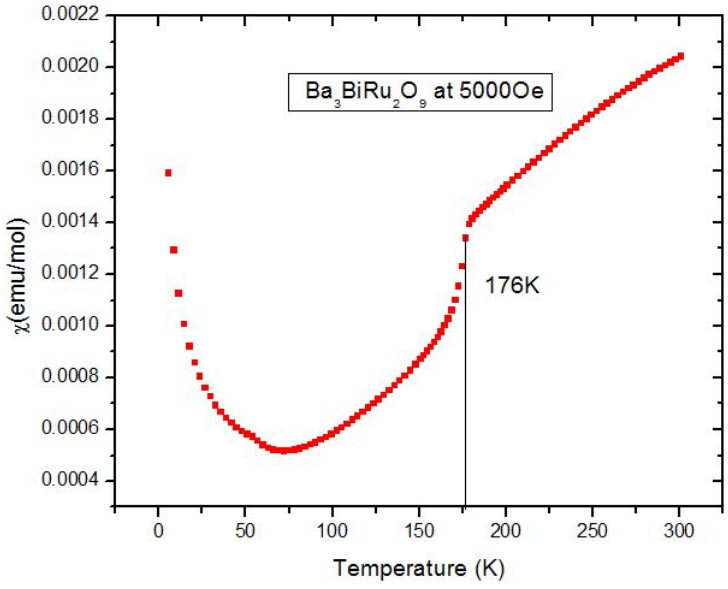

Figure 4.3: Magnetic susceptibility dependence on temperature for $Ba_3BiRu_2O_9$

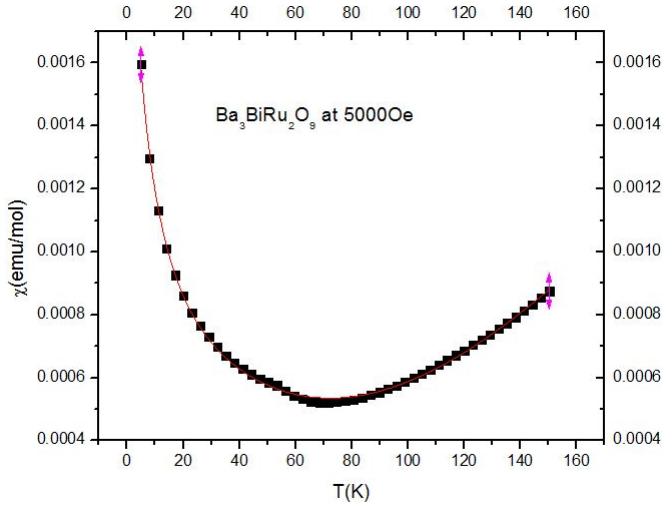

Figure 4.4: Fitting the Magnetic susceptibility dependence on temperature for spin gap in $Ba_3BiRu_2O_9$. $\chi(T) = \chi_{sg} + \chi_0 + C/T - \theta$. The obtained spin gap value is 314.27K

due to the reported susceptibility of an isolated dimer(Ru_2O_9 dimer), which increases more rapidly than susceptibility decrease of a conventional paramagnet following Curie-Weiss law[27]. Hence the combined susceptibility of an dimer and Curie-Weiss fit is seen to increase. A fit is also performed in the temperature range 2-150K with the equation[27]:

$$\chi(T) = \chi_{sg} + \chi_0 + C/T - \theta \tag{4.1}$$

$$\chi_{sg} = aT^{.5}exp(-\Delta/K_BT) \tag{4.2}$$

here Δ_{sg} is the spin gap. Fig4.4 shows the fitting of susceptibility data with the spin gap equation 4.1. The spin gap value obtained from the least square fitting is $\Delta_{sg} = 314.27K$. Other parameters obtained from the fit are: $a = 3.096 * 10^{-4}emu/mol/k^{.5}$, $\chi_o = 3.206 * 10^{-4}emu/mol$, $C = .01417emu/mol/K$ and $\theta = -6.23K$. The spin-gap value was also calculated at the fields 1000 Oe and 500 Oe. The obtained spin gap value remained the same.

4.3 Specific Heat Measurements

The signature of structural dimerization could also be seen as the anomaly in the specific heat data shown in fig4.5 taken at different

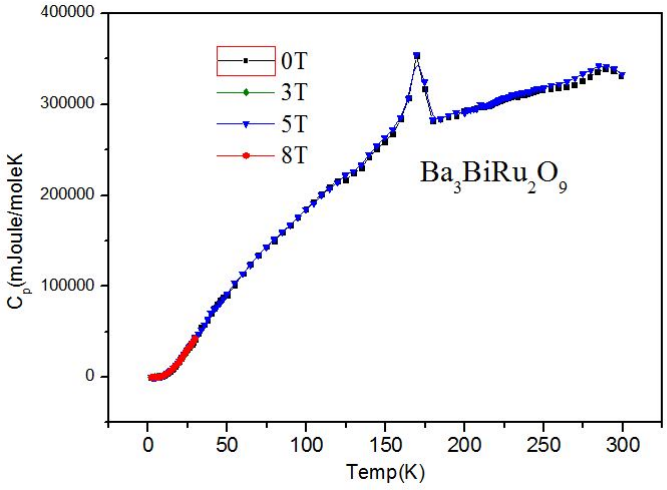

Figure 4.5: Specific heat dependence on temperature at various magnetic fields. Anomaly at 175k corresponding to magnetoelastic spin gap transition

fields. The anomaly corresponds to the spin gap transition temperature at 175K. The anomaly in the specific heat data is due to the reported magnetoelastic transition at the same temperature[27]. There is a discontinuous change in the inter-dimer distance (Ru-Ru) across the transition leading to the observed anomaly in the specific heat data. Fig4.6 shows the C_p/T^3 dependence on temperature for $Ba_3BiRu_2O_9$. These measurements were done at 0T, 3T, 5T and 8T in TIFR, Bombay. It shows a peak at around 10K with a change in curvature below 7.6K. This kind of non-Debye behavior was also seen in $Ba_3CoRu_2O_9$. Although this behavior is qualitatively similar to that of well studied conventional glass materials, but the reason as to why this is visible in these triple perovskite ruthenates is unknown.

4.4 Dielectric Measurements

The real part of dielectric susceptibility with respect to temperature at different frequency is plotted in the fig4.7. We observe a peak at the transition temperature 175K. Below this temperature there is a sharp decrease in the susceptibility indicating the possibility of a strong magneto-dielectric coupling in the system. The $tan\delta$ plot shown in the fig4.8 shows a frequency dependent behavior. This behavior is a signature of relaxor ferroelectric. The Vogel-Fulcher fit have been done(see

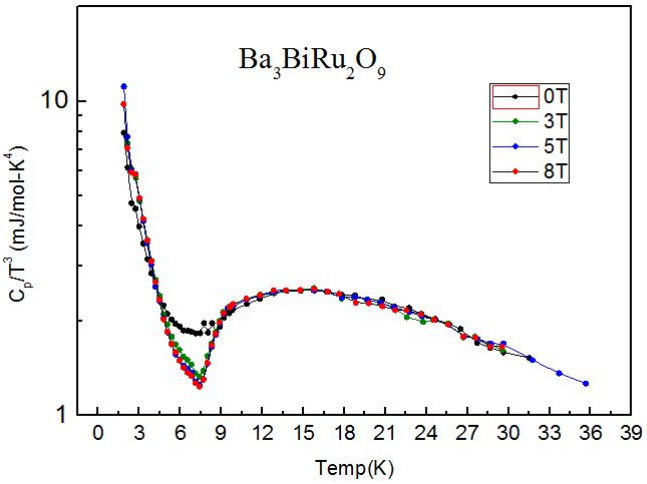

Figure 4.6: C_p/T^3 versus T plot for $Ba_3BiRu_2O_9$ at various fields. There is an upturn below 5K, indicating the non-Debye behavior at this temperature.

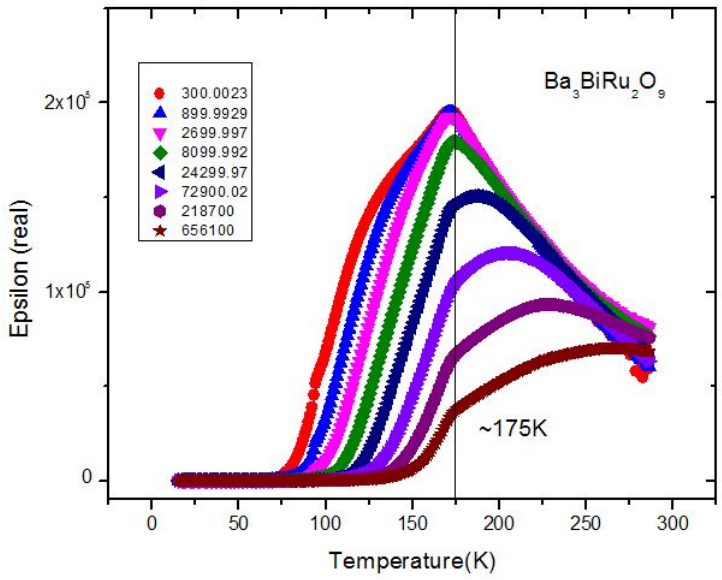

Figure 4.7: Real part of dielectric susceptibility dependence on temperature.Peak at magnetic transition temperature along with subsequent drop.

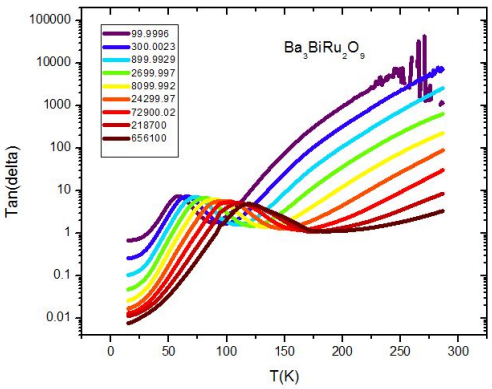

Figure 4.8: $Tan\delta$ plot with respect to temperature for $Ba_3BiRu_2O_9$ showing relaxor like behavior below transition temperature.

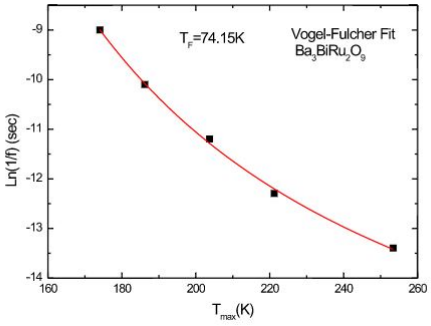

Figure 4.9: Vogel-Fulcher fit for the frequency dependence on T_{max} from the dielectric spectrum of $Ba_3BiRu_2O_9$.

fig4.9). The freezing temperature is about 74K. So $Ba_3BiRu_2O_9$ is a relaxor ferroelectric with a possibility of magneto-dielectric coupling at the transition temperature. This behavior in the system is due to the unconventional oxidation state of bismuth ($+4$). $+4$ Oxidation state of bismuth is uncommon because the valence shell configuration of $5d^{10}6s^1$ is unstable. It can either undergo disproportionation to Bi^{+3} + Bi^{+5} or it can undergo charge transfer to Ru^{+4} forming $Ru^{+4.5}$ + Bi^{+3}[27]. BVS calculations and neutron powder data show no evidence for disproportionation or charge transfer[27]. Bi^{+4}acts as a transient charge reservoir communicating changes in the isolated Ru_2O_9 dimers, thereby facilitating a first order transition[27]. Due to the high polarizibility of the 6s electrons in the valence shell there could be a small dipole

moment induced in the bismuth octahedra. As the bismuth octahedra are separated by the Ru_2O_9 dimers, hence the long range order among the dipoles may not form due to spatial separation, leading to the formation of polarized nano-regions(PNRs). There is no formal proof for this assertion. This assertion has to be further investigated.

Chapter 5

Summary And Future Work

5.1 Summary

Polycrystalline samples of $Ba_3CoRu_2O_9$ and $Ba_3BiRu_2O_9$ have been prepared using solid state ceramic route. Structural characterization of the compounds has been done using Rietveld analysis. These compounds have Ru_2O_9 dimers interconnected by metal oxide octahedra. Magnetic property investigations show that $Ba_3CoRu_2O_9$ undergoes an anti-ferromagnetic transition at 108K and for $Ba_3BiRu_2O_9$ there is a spin gap transition at 175K. Specific heat measurements show anomalies corresponding to the magnetic transition temperature. The dielectric measurements on both the samples are done. They show a possibility of strong magneto-dielectric coupling at the transition temperature. $Ba_3BiRu_2O_9$ shows a possible relaxor like behavior below the transition temperature.

The C_p/T^3 dependence with temperature shows a peak at around 10K for $Ba_3BiRu_2O_9$ and at 22K for $Ba_3CoRu_2O_9$. This kind of signature of peak in C_p/T^3 is a feature of glassy-like behavior. Such a kind of glassy state for example has been seen in half-doped manganites[33]. The reason for such an unusual behavior in these samples is unknown. This has to be further investigated.

5.2 Future Plans

- To do the Rietveld refinement of neutron data of $Ba_3CoRu_2O_9$ to get the complete magnetic structure below the transition temperature.
- To find out the magnetoelectric coupling, magneto-dielectric measurements needs to be done along with polarization measurements to conclude if there is a coupling and if these systems are multiferroic.
- Also to look into the possibility of glassy like behavior in these compounds.

References

[1] W. J. Merz, Phys. Rev. 76 (1949) 1221–1225. doi:10.1103/PhysRev.76.1221.

[2] J. C. Slater, The Journal of Chemical Physics 9 (1941) 16–33. doi:http://dx.doi.org/10.1063/1.1750821.

[3] D. et al, Journal of Applied Physics 68 (6) (1990) 2916–2921. doi:http://dx.doi.org/10.1063/1.346425.

[4] G. Burns, F. Dacol, Solid State Communications 48 (10) (1983) 853 – 856. doi:http://dx.doi.org/10.1016/0038-1098(83)90132-1.

[5] A. Pelaiz-Barranco, 2013, Ch. Chapter 5, pp. 85–102.

[6] M. I. Desheng Fu, Hiroki Taniguchi, S. Mori, Advances in ferroelectrics.

[7] C. Sang-Wook, M. Maxim, Nat Mater 6 (2007) 1476–11227. doi:10.1038/nmat1804.

[8] M. Bibes, A. Barthelemy, Nat Mater 7 (2008) 425–426.

[9] M. e. a. Gajek, Nat Mater 6 (2007) 296–302.

[10] J. Kreisel, M. Kenzelmann, Europhysics News 40 (2009) 17 – 20. doi:http://dx.doi.org/10.1051/epn/2009702.

[11] N. A. Hill, The Journal of Physical Chemistry B 104 (29) (2000) 6694–6709. doi:10.1021/jp000114x.

[12] D. Khomskii, APS Physics 2,20 (2009).

[13] J. van den Brink, D. I. Khomskii, Journal of Physics: Condensed Matter 20 (43) (2008) 434217.

[14] T. Kimura, Annual Review of Materials Research 37 (1) (2007) 387–413. doi:10.1146/annurev.matsci.37.052506.084259.

[15] T. Kimura, Nature 426 (2003) 55–58.

[16] M. Mostovoy, Phys. Rev. Lett. 96 (2006) 067601. doi:10.1103/PhysRevLett.96.067601.

[17] H.-C. zur Loye et al, Journal of the American Chemical Society 124 (46) (2002) 13877–13885. doi:10.1021/ja0271781.

[18] C. et al, Phys. Rev. B 58 (1998) 10315–10318. doi:10.1103/PhysRevB.58.10315.

[19] M. et al, Nature 396 (1998) 658–660.

[20] J. M. Longo, P. M. Raccah, J. B. Goodenough, Journal of Applied Physics 39 (2) (1968) 1327–1328. doi:http://dx.doi.org/10.1063/1.1656282.

[21] P. Khalifah 297 (5590) (2002) 2237–2240. doi:10.1126/science.1075556.

[22] P. Khalifah, Nature 411 (2001) 669–671.

[23] H. D. Zhou, A. Kiswandhi, Y. Barlas, J. S. Brooks, T. Siegrist, G. Li, L. Balicas, J. G. Cheng, F. Rivadulla, Phys. Rev. B 85 (2012) 041201. doi:10.1103/PhysRevB.85.041201.

[24] W.-J. Son, P. Manuel, D. Adroja, M.-H. Whangbo, Inorganic Chemistry 50 (19) (2011) 9400–9405. doi:10.1021/ic201023j.

[25] A. Y. et.al., Journal of the Physical Society of Japan 76 (4) (2007) 043703. doi:10.1143/JPSJ.76.043703.

[26] J. Hwang, E. S. Choi, F. Ye, C. R. Dela Cruz, Y. Xin, H. D. Zhou, P. Schlottmann, Phys. Rev. Lett. 109 (2012) 257205. doi:10.1103/PhysRevLett.109.257205.

[27] M. et.al., Phys. Rev. B 84 (2011) 220406. doi:10.1103/PhysRevB.84.220406.

[28] Z. Huang, M. Avdeev, B. Kennedy, K. Knight, Q. Zhou, C. Ling, Journal of Physics: Condensed Matter 26 (27) (2014) 276003.

[29] H. M. Rietveld, Acta Crystallographica 22 (1) (1967) 151–152. doi:10.1107/S0365110X67000234.

[30] R. Young, Oxford university press, 1993.

[31] Scanning Electron Microscope A to Z. Basic Knowledge For Using The SEM. .
URL http://www.jeol.co.jp/en/applications/pdf/sm/sem_atoz_all.pdf

[32] Ppms manual.

[33] A. Banerjee, R. Rawat, K. Mukherjee, P. Chaddah, Phys. Rev. B 79 (2009) 212403. doi:10.1103/PhysRevB.79.212403.